

Over-the-Air Learning-based Geometry Point Cloud Transmission

Chenghong Bian, *Student Member, IEEE*, Yulin Shao, *Member, IEEE*, and Deniz Gündüz, *Fellow, IEEE*

Abstract—3D point cloud is a three-dimensional data format generated by LiDARs and depth sensors, and is being increasingly used in a large variety of applications from autonomous vehicles to robotics and metaverse. This paper presents novel solutions for the efficient and reliable transmission of point clouds over wireless channels for real-time applications. We first propose SEPT for the transmission of small-scale point clouds, which encodes the point cloud via an iterative downsampling and feature extraction process. At the receiver, SEPT decoder reconstructs the point cloud with latent reconstruction and offset-based upsampling. A novel channel-adaptive module is proposed to allow SEPT to operate effectively over a wide range of channel conditions. Next, we propose OTA-NeRF, a scheme inspired by neural radiance fields. OTA-NeRF performs voxelization to the point cloud input and learns to encode the voxelized point cloud into a neural network. Instead of transmitting the extracted feature vectors as in the SEPT scheme, it transmits the learned neural network weights over the air in an analog fashion along with few hyperparameters that are transmitted digitally. At the receiver, the OTA-NeRF decoder reconstructs the original point cloud using the received noisy neural network weights. To further increase the bandwidth efficiency of the OTA-NeRF scheme, a fine-tuning algorithm is developed, where only a fraction of the neural network weights are retrained and transmitted. Extensive numerical experiments confirm that both the SEPT and the OTA-NeRF schemes achieve superior or comparable performance over the conventional approaches, where an octree-based or a learning-based point cloud compression scheme is concatenated with a channel code. As an additional advantage, both schemes mitigate the cliff and leveling effects making them particularly attractive for highly mobile scenarios, where accurate channel estimation is challenging if not impossible.

Index Terms—Deep joint source channel coding (DeepJSCC), point cloud, over-the-air, neural radiance field (NeRF).

I. INTRODUCTION

3D point clouds are collections of three-dimensional data points and their associated attributes, such as color, temperature, and normals [2]–[4]. Generated through technologies such as light detection and ranging (LiDAR), depth camera, and structured light scanning, point clouds are non-ordered and non-uniformly distributed within space. Point clouds have found applications in a wide range of scenarios from environmental monitoring to biomedical imaging, autonomous driving and agriculture.

In many cases, point clouds are captured by remote devices, and are communicated for processing where the necessary computing resources are available. Therefore, wireless

transmission plays a vital role in facilitating the mobility and accessibility of 3D point clouds, empowering industries and applications reliant on this expressive data format. The standard approach for point cloud transmission consists of two main steps, where octree-based point cloud compression [2] is followed by digital transmission over the wireless link. The standard approach faces several challenges in achieving accurate and reliable transmission of 3D point cloud data, namely, inefficient feature extraction due to the limitation of the octree representation in extracting contextual features from the 3D point cloud data, and the cliff and leveling effects, which are inherent to the digital transmission of the extracted features.

There has been significant progress in recent years thanks to the adoption of learning-based algorithms and neural network architectures for point cloud classification, semantic segmentation [3]–[7], and compression [8]–[11]. In particular, the authors in [3] propose PointNet that uses permutation-invariant operations, such as pointwise multilayer perceptrons (MLPs) and max-pooling, to extract features for point cloud classification and segmentation. The follow-up works improve the classification and segmentation performances by using more advanced operations such as 3D convolution (KPconv) [5] and self-attention [4], [6], [7]. Meanwhile, various deep learning-based schemes have been proposed for point cloud compression [8]–[13]. Among them, the authors in [8] use neural networks to predict the occupancy probability for a certain node in the octree and adopt an entropy model to generate the compression output. Ref. [10] uses multiple KPconv [5] and downsampling layers to progressively extract information, and adopts an offset-based up-sampling algorithm to reconstruct the point cloud at the decoder. The authors in [11] follow the framework in [10] and use the point cloud transformer [6] as the backbone to enhance the compression performance.

Recently, neural radiance fields (NeRFs) [14], [15] have presented a new perspective for point cloud compression. Originally proposed in [14], NeRF aims to represent a 3D scene using a neural network whose weights are trained to overfit a single input sample. Once trained, the NeRF model is capable to provide high quality reconstructions of the same source from different angles. Following the idea of NeRF, the authors in [13] represent each part of the point cloud using a neural network along with a latent code. The neural network is trained to predict the occupancy information of a voxel given its x , y and z coordinates. The follow-up work [12] improves the rate-distortion (R-D) performance in [13] by adopting the state-of-the-art neural network compression algorithm [16] and extends the framework to tackle more

The authors are with the Department of Electrical and Electronic Engineering, Imperial College London, London SW7 2AZ, U.K. (e-mail: {c.bian22,y.shao,d.gunduz}@imperial.ac.uk).

This paper has been presented in part at the IEEE International Workshop on Signal Processing Advances in Wireless Communications, 2024 [1].

challenging attribute compression of the point cloud. Both schemes are reported to outperform the benchmark geometry-based point cloud compression (G-PCC) algorithm [17].

Another direction to facilitate the wireless transmission of point clouds is to employ joint source-channel coding [18], which would mitigate the cliff and leveling effects, which the conventional separation-based architectures suffer from. Deep joint source channel coding (DeepJSCC), originally proposed in [19], utilizes analog transmission to mitigate these problems. Over the years, there has been a growing interest in utilizing DeepJSCC to develop semantic communication systems [20]. In particular, researchers have actively applied DeepJSCC to different wireless channels, e.g., multi-path fading [21], MIMO [22], and relay channels [23], as well as different data modalities, e.g., image [24], video [25], [26] and speech [27]. Recently, it is shown in [28] that DeepJSCC is also applicable to efficient transmission of neural network weights over the wireless channel. In particular, the authors in [28] train a neural network, dubbed AirNet, which takes both the classification accuracy as well as the noisy wireless channel into account and formulate it as a DeepJSCC problem. The neural network weights are directly transmitted over the channel thus avoiding the cliff and leveling effects. It is shown that AirNet achieves higher classification accuracy compared with the digital base-lines using less number of channel uses.

Despite the importance of wireless delivery in enabling many point cloud applications, only a few papers investigate the wireless point cloud transmission problem [1], [29]–[32]. In particular, our previous work, [1] directly maps the point cloud into a latent vector, which is transmitted directly over the channel. The authors in [30] adopts a hybrid digital-analog transmission approach, where the point cloud is first compressed using octree-based point cloud compression algorithm and the compressed bits are transmitted using digital coded modulation. They then adopt the graph Fourier transform to encode the residual information, which is transmitted in an analog fashion. The same authors further introduce a graph convolutional neural network for more efficient geometric feature extraction in [31], and employ the NeRF method to efficiently encode the graph information in [32]. Though digital coded modulation is still required to deliver side information for successful reconstruction at the decoder, these schemes can achieve modest reconstruction performance while mitigating cliff and leveling effects. Another related work is [33], where the authors extend our previous work [1] by digitally transmitting additional coordinate information to achieve superior reconstruction performance.

In this paper, we first leverage the recent advances in point cloud processing [4], [5], especially in point cloud compression [9]–[11], in the context of deep joint source-channel coding (DeepJSCC) [19] to develop the SEPT (SEmantic Point cloud Transmission) framework, which is designed for small-scale point cloud transmission over bandwidth limited channels. At the transmitter, SEPT encoder maps the point cloud directly into a latent vector without voxelization using the point transformer [4] as its backbone. At the receiver, instead of feeding the noisy latent vector directly into the up-sampling layers, we introduce a refinement layer to first denoise the latent

vector. Finally, offset-based up-sampling layers are employed for point cloud reconstruction. We further introduce a signal-to-noise-ratio (SNR)-adaptive (SA) module for adaptation to channel variations, through which we train a single pair of SEPT encoder and decoder that can operate over a wide range of channel conditions.

While SEPT is designed mainly for small scale point clouds, we further propose the OTA-NeRF framework for the transmission of more complex point clouds. The OTA-NeRF first voxelizes the input point cloud and feeds the coordinates of the voxelized input to the OTA-NeRF network to produce the occupancy probabilities for reconstruction. Note that a specific neural network is trained to represent each point cloud input, whose weights are transmitted directly over the wireless channel. Similarly to AirNet [28], noise injection during training is used to enable robustness against channel noise. To further increase the bandwidth efficiency, we only re-train and transmit the difference in the neural network weights with respect to a base model that is available to the receiver. Extensive numerical experiments show that employing such a base model improves the distortion-bandwidth trade-off, while also reducing the encoding complexity compared with the original OTA-NeRF scheme.

Our main contributions can be summarized as follows:

- We present SEPT for the efficient delivery of small-scale 3D point clouds over static and fading wireless channels. The SEPT encoder directly maps the input point cloud into a latent vector with fully analog transmission. We show that SEPT achieves significant performance gains over the digital benchmarks for the delivery of small-scale point clouds over bandwidth-limited wireless links, targeting real-time applications.
- We introduce novel SNR-adaptive encoding and decoding modules for SEPT. This module differs from the attention-based designs in [22], [34] for SNR-adaptive image transmission. In particular, the mean-pooling operation calculates the average of the features belonging to different points following the permutation invariance of point clouds.
- To facilitate the transmission of larger point clouds, the OTA-NeRF framework is proposed, where each point cloud input is represented by a specific neural network. The neural network is trained to minimize the reconstruction loss, and its weights are transmitted over the wireless channel in an analog fashion along with a limited number of hyperparameters, which are transmitted digitally using channel codes.
- To further improve the performance of the proposed OTA-NeRF framework, we consider a fine-tuning approach, where, to transmit different point clouds, only a fraction of the neural network weights need to be re-trained and transmitted, leading to an improved bandwidth-distortion trade-off, as well as a reduction in the encoding complexity.
- Extensive simulations verify that the proposed SEPT and OTA-NeRF schemes outperform or achieve comparable reconstruction performance with respect to (w.r.t.) the fully digital benchmarks that first compress the point

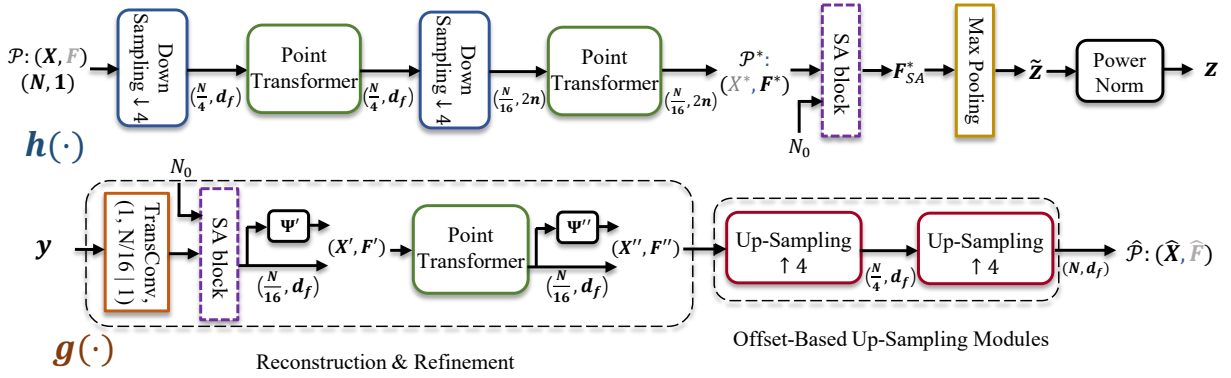


Figure 1: The detailed architecture of SEPT with an encoder $h(\cdot)$ and a decoder $g(\cdot)$. For clarity, we label the dimension information of the point cloud after each processing module. As an example, in $(\frac{N}{4}, d_f)$ after the first point transformer at the encoder, $\frac{N}{4}$ refers to the number of points after the point transformer and d_f is the dimension of the feature vectors. The coordinate reconstruction modules as denoted as Ψ' and Ψ'' . The SA block, which takes the feature tensor and the noise variance N_0 as input, is designed for SNR-adaptive point cloud transmission.

cloud using G-PCC or other learning-based algorithms, and transmit the compressed bits using digital coded modulations. More importantly, both schemes eliminate/mitigate the cliff and leveling effects, which makes them particularly appealing to be deployed in highly mobile scenarios, where accurate channel estimation is not feasible or very costly.

II. SYSTEM MODEL

A point cloud can be expressed as $\mathcal{P} = (\mathbf{X}, \mathbf{F})$, where $\mathbf{X} \triangleq \{\mathbf{x}_i \in \mathbb{R}^3\}$, $i \in [N]$, is a set of N points in space, and $\mathbf{F} \triangleq \{\mathbf{f}_i \in \mathbb{R}^d\}$, $i \in [N]$, is a set of features associated with each point in \mathbf{X} . In this paper, we consider point clouds with no input attributes¹ and focuses on transmitting only the coordinates in \mathbf{X} . Following the convention, we set the input attributes \mathbf{F} to an all-ones vector with $d = 1$.

The encoder maps the input 3D point cloud \mathcal{P} to a channel codeword, $\mathbf{z} \in \mathbb{C}^n$, where n is the available channel bandwidth. The channel use per point (CPP) is given by $\frac{n}{N}$. We impose a power constraint on transmitted codewords:

$$\|\mathbf{z}\|_2^2 \leq nP. \quad (1)$$

The received signal $\mathbf{y}' \in \mathbb{C}^n$ is expressed as:

$$\mathbf{y}' = h\mathbf{z} + \mathbf{v}, \quad (2)$$

where $\mathbf{v} \in \mathbb{C}^n$ denotes a complex additive white Gaussian noise (AWGN) vector with independent and identically distributed elements, $\mathbf{v} \sim \mathcal{CN}(\mathbf{0}, N_0 \mathbf{I}_n)$. When h is a constant, the wireless channel in (2) degrades to an AWGN channel. The average SNR is defined as $\text{SNR} = 10 \log_{10} \frac{|h|^2 P}{N_0}$. Without loss of generality, we assume $P = 1$ in the sequel.

We also consider a slow fading channel, where h is modeled as a random variable, which takes an independent realization from an underlying distribution for the transmission of each

point cloud. We assume that both the transmitter and the receiver have perfect knowledge on the channel state information (CSI), h . Upon receiving \mathbf{y}' , the decoder equalizes it using h as in [23]. Then, the equalized signal is converted to a real vector $\mathbf{y} \in \mathbb{R}^{2n}$ which is utilized in the subsequent decoding process to obtain the reconstructed point cloud $\hat{\mathcal{P}}$.

Two conventional peak signal-to-noise ratio (PSNR) measures [35], D1 and D2, are adopted to evaluate the reconstruction quality. For point clouds \mathcal{A} and \mathcal{B} , $D1(\mathcal{A}, \mathcal{B})$ measures the average point-to-point geometric distance between each point in point cloud \mathcal{A} and its nearest neighbor in point cloud \mathcal{B} . To be precise, we first calculate the mean squared error, $e_{\mathcal{A}, \mathcal{B}}^{D1}$:

$$e_{\mathcal{A}, \mathcal{B}}^{D1} \triangleq \frac{1}{N} \sum_{\mathbf{a}_i \in \mathcal{A}} \|\mathbf{a}_i - \mathbf{b}_k\|_2^2, \quad (3)$$

where $k = \arg \min_{j \in [N]} \|\mathbf{a}_i - \mathbf{b}_j\|_2^2$.

Then, D1 is defined as [35]:

$$D1(\mathcal{A}, \mathcal{B}) \triangleq 10 \frac{3\gamma^2}{\max(e_{\mathcal{A}, \mathcal{B}}^{D1}, e_{\mathcal{B}, \mathcal{A}}^{D1})}, \quad (4)$$

where factor 3 in the numerator is due to the 3D coordinates used in the representation, and the peak value, γ , is set to unity due to the fact that the input points are normalized within the range $[0, 1]$. Similarly, D2 evaluates the point-to-plane distance between point clouds \mathcal{A} and \mathcal{B} and the error term for D2 is defined as:

$$e_{\mathcal{A}, \mathcal{B}}^{D2} = \frac{1}{N} \sum_{\mathbf{a}_i \in \mathcal{A}} (\mathbf{a}_i - \mathbf{b}_k) \cdot \mathbf{n}_i, \quad (5)$$

where \mathbf{n}_i is the normal vector corresponding to \mathbf{a}_i and \mathbf{b}_k is the nearest neighbor of \mathbf{a}_i in \mathcal{B} . After obtaining (5), we follow the same formula in (4) to calculate $D2(\mathcal{A}, \mathcal{B})$.

III. SEPT FRAMEWORK

This section details the design of the encoding and decoding functions for the SEPT framework, originally proposed in [1].

¹Nevertheless, the point clouds in the intermediate layers of SEPT can have non-trivial attributes/features. For example, the neighboring information is contained in the attributes of the downsampled points.

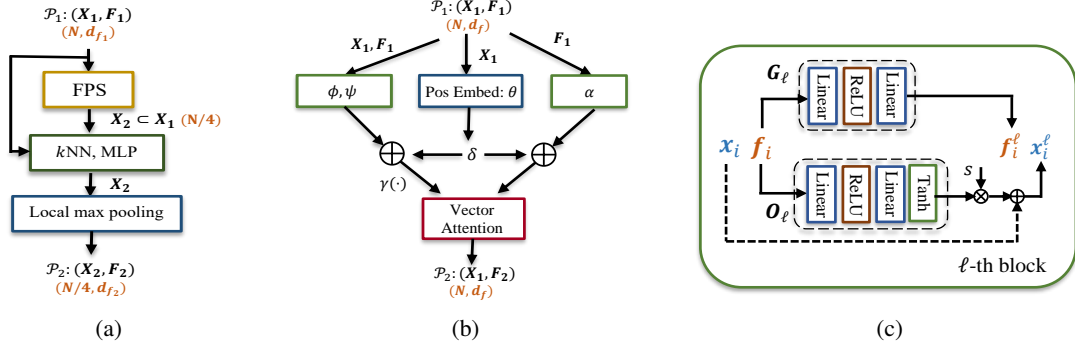


Figure 2: The inner architectures of (a) the downsampling module, (b) the point transformer layer, and (c) the ℓ -th block of the offset-based up-sampling module, $\ell \in [1, L]$.

To make the SEPT framework practically relevant, we also introduce a novel SNR-adaptive module for SEPT to achieve the reconstruction performance obtained by separately trained models. The detailed architecture of SEPT is presented in Fig. 1.

A. SEPT Encoder

The encoder of SEPT consists of three main modules: downsampling, self-attention, and max pooling.

Downsampling. The objective of the downsampling module is to reduce the number of points in the input point cloud. Let $\mathcal{P}_1 = (\mathbf{X}_1, \mathbf{F}_1)$ and $\mathcal{P}_2 = (\mathbf{X}_2, \mathbf{F}_2)$ denote the input and output point clouds of a downsampling module, respectively, where $\mathbf{X}_2 \subset \mathbf{X}_1$. As shown in Fig. 2(a), the proposed SEPT uses the farthest point sampling² (FPS) algorithm to generate the down-sampled geometric information, \mathbf{X}_2 . To generate the feature vector of the i -th point in \mathbf{X}_2 , denoted by $\mathbf{f}_i^{(2)} \in \mathbb{R}^{d_{f_2}}$, we first find its k -nearest neighbors within a given radius r in \mathbf{X}_1 , denoted by $\mathbb{N}(i)$.³ Then, we concatenate the feature vectors of the points in $\mathbb{N}(i)$ with their coordinates and organize them into a tensor, denoted by $\mathbf{T}_{\mathbb{N}(i)} \in \mathbb{R}^{(d_{f_1}+3) \times k \times N_1}$ where N_1 denotes the cardinality of \mathbf{X}_1 , and feed this tensor to a 2D convolutional layer followed by batch normalization, ReLU, and max pooling. In each downsampling module, we set the cardinality of \mathbf{X}_2 to be 1/4 of that of \mathbf{X}_1 , i.e., $|\mathbf{X}_2| = |\mathbf{X}_1|/4$.

Self-Attention Module. In SEPT, each downsampling module is followed by a self-attention module [4], a point cloud processing technique that is capable of extracting rich neighboring information. Denote the input and output point clouds of the self-attention layer by $\mathcal{P}_1 = (\mathbf{X}_1, \mathbf{F}_1)$ and $\mathcal{P}_2 = (\mathbf{X}_1, \mathbf{F}_2)$, respectively. As shown in Fig. 2(b), the self-attention layer refines the features of each point in \mathcal{P}_1 . The inner operations can be written as

$$\mathbf{f}_i^{(2)} = \sum_{j \in \mathbb{N}(i)} \text{Softmax}(\gamma(\phi(\mathbf{f}_i^{(1)}) - \phi(\mathbf{f}_j^{(1)})) + \delta(\mathbf{x}_i, \mathbf{x}_j)) \odot (\alpha(\mathbf{f}_j^{(1)}) + \delta(\mathbf{x}_i, \mathbf{x}_j)), \quad (6)$$

²In principle, we can directly generate the encoded vectors without using the FPS. However, this would cause significant computation complexity and performance loss which is observed in our experiments.

³If the i -th ($i < k$) neighbor has a distance larger than r from the sampled point, we will use the nearest neighbor to replace it.

where $\mathbf{f}_i^{(1)}$ and $\mathbf{f}_i^{(2)}$ denotes the original and the refined feature vectors of the i -th point, respectively; $\gamma, \phi, \alpha : \mathbb{R}^{d_f} \rightarrow \mathbb{R}^{d_f}$ are realized by MLPs where d_f is the feature dimension; $\delta(\mathbf{x}_i, \mathbf{x}_j) = \theta(\mathbf{x}_i - \mathbf{x}_j)$ is the positional information and $\theta : \mathbb{R}^3 \rightarrow \mathbb{R}^{d_f}$ is an MLP layer for positional embedding; \odot denotes the element-wise product. That is, we adopt vector attention [4], as opposed to the standard scalar dot-product attention used in language and vision transformer models, for better performance.

As shown in Fig. 1, after two consecutive downsampling and self-attention module pairs, the final downsized point cloud is obtained, which we denote by $\mathcal{P}^* = (\mathbf{X}^*, \mathbf{F}^*)$, where $\mathbf{X}^* \in \mathbb{R}^{(N/16) \times 3}$ and $\mathbf{F}^* \in \mathbb{R}^{(N/16) \times 2n}$. Note that n is the length of the transmitted codeword, \mathbf{z} in (1). We emphasize that the features \mathbf{F}^* are generated by neural networks and can be optimized to be robust to noise, thanks to end-to-end learning. On the other hand, the coordinates \mathbf{X}^* are obtained from FPS and are susceptible to noise. Our empirical results indicate that \mathbf{X}^* has to be transmitted to the receiver reliably via digital communications. Failure to do so results in a substantial degradation in the reconstruction performance of the point cloud. Digital transmission of \mathbf{X}^* , however, would cause two problems: 1) the cliff and leveling effects; and 2) excessive channel usage. To mitigate these problems, SEPT completely eliminates the need to transmit the coordinate tensor (\mathbf{X}^*), and instead focuses solely on transmitting the features (\mathbf{F}^*) to the receiver. To be precise, SEPT learns to encode the global features in \mathbf{F}^* as the transmitted channel codeword, and the decoder is trained to reconstruct the entire point cloud from the noisy channel output without the aid of its coordinate tensor. By doing so, SEPT significantly reduces the amount of data that needs to be transmitted, leading to more efficient and streamlined communication.

Max Pooling. The last step⁴ at the encoder is to transform $\mathbf{F}^* \in \mathbb{R}^{(N/16) \times 2n}$ to the latent vector $\tilde{\mathbf{z}} \in \mathbb{R}^{2n}$. This is done by applying max pooling over the $N/16$ points to generate the $2n$ -dimensional vector $\tilde{\mathbf{z}}$ which will be further converted to the complex codeword $\mathbf{z} \in \mathbb{C}^n$ defined in (1).

⁴The input to the max pooling module will be \mathbf{F}_{SA}^* if the SA module is adopted.

B. SEPT Decoder

The decoder of SEPT consists of two modules: latent reconstruction and refinement, and offset-based up-sampling.

Latent Reconstruction and Refinement. The latent reconstruction module takes the noisy channel output as input to reconstruct \mathcal{P}^* . As shown in Fig. 1, given the received signal \mathbf{y} , we first use a TransConv layer, which is essentially a 1D deconvolution with a unit stride, to generate the initial estimate of \mathbf{F}^* , denoted by $\mathbf{F}' \in \mathbb{R}^{(N/16) \times 2n}$. Then, we employ a coordinate reconstruction module $\Psi' : \mathbb{R}^{2n} \rightarrow \mathbb{R}^3$, which is composed of MLP layers and a ReLU function, and operates on each row of \mathbf{F}' to generate an initial estimate of the coordinates:

$$\mathbf{X}' = \Psi'(\mathbf{F}'), \quad (7)$$

where $\mathbf{X}' \in \mathbb{R}^{(N/16) \times 3}$. The initial estimates $(\mathbf{X}', \mathbf{F}')$ can be erroneous due to noise. Therefore, we further use a self-attention module, to refine the features:

$$\mathbf{F}'' = \text{Self-Attention}(\mathbf{X}', \mathbf{F}'). \quad (8)$$

Next, a new coordinate reconstruction layer, Ψ'' , is applied to \mathbf{F}'' to produce a refined estimation of coordinates, \mathbf{X}'' . Our refinement module is shown to be very effective in denoising the coordinates and features.

Offset-Based Up-Sampling. Finally, we employ an offset-based up-sampling module [10] on $(\mathbf{X}'', \mathbf{F}'')$ for point cloud reconstruction. For the i -th point in the input point cloud, whose coordinates and features are denoted by $(\mathbf{x}_i, \mathbf{f}_i)$, this module generates L new points $\{(\mathbf{x}_i^\ell, \mathbf{f}_i^\ell), \ell \in [1, L]\}$ as:

$$\mathbf{x}_i^\ell = \mathbf{x}_i + s \cdot O_\ell(\mathbf{f}_i), \quad (9)$$

$$\mathbf{f}_i^\ell = G_\ell(\mathbf{f}_i), \quad (10)$$

where $O_\ell : \mathbb{R}^{d_f} \rightarrow [-1, 1]^3$ is an MLP layer followed by a tanh function that aims to generate an offset vector; G_ℓ is comprised of MLPs and a ReLU function that maps the input feature to a new one with the same dimension; and s is a scaling factor for the offsets. Compared with [10], SEPT uses a relatively large scaling factor $s = 0.1$ to give the up-sampling module more freedom for better performance, considering the additional noise introduced by the wireless channel. The detailed architectures for O_ℓ and G_ℓ are shown in Fig. 2(c).

In SEPT, we use two up-sampling modules, and L is set to 4 in each module to match the encoder operations. Denoting by $\hat{\mathcal{P}} = (\hat{\mathbf{X}}, \hat{\mathbf{F}})$ the final output of the up-sampling modules, the Chamfer distance between \mathbf{X} and $\hat{\mathbf{X}}$, denoted by $d_{cd}^2(\mathbf{X}, \hat{\mathbf{X}})$, is used as the loss function:

$$\mathcal{L}_{CD} = \frac{1}{N} \sum_{\mathbf{x} \in \mathcal{P}} \min_{\mathbf{y} \in \hat{\mathcal{P}}} \|\mathbf{x} - \mathbf{y}\|_2^2 + \frac{1}{N} \sum_{\mathbf{y} \in \hat{\mathcal{P}}} \min_{\mathbf{x} \in \mathcal{P}} \|\mathbf{y} - \mathbf{x}\|_2^2. \quad (11)$$

C. SNR-adaptive (SA) Module

We next describe the design for our SNR-adaptive module, which is shown in Fig.1.

At the SEPT encoder, the SA block takes the feature tensor, $\mathbf{F}^* \in \mathbb{R}^{\frac{N}{16} \times 2n}$ as input and adopts mean pooling along the

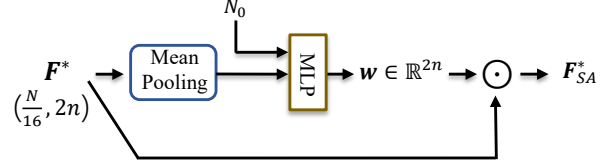


Figure 3: The proposed SA module for SNR-adaptive point cloud transmission.

first dimension. This generates an n -dimensional vector which is concatenated with the noise variance, N_0 , and fed to an MLP layer, whose output is a weight vector $\mathbf{w} \in \mathbb{R}^{2n}$. The vector is repeated $\frac{N}{16}$ times along the first dimension to obtain a matrix $\mathbf{W} \in \mathbb{R}^{\frac{N}{16} \times 2n}$, which will be multiplied with \mathbf{F}^* in an element-wise manner. The entire operation at the SEPT encoder is shown in Fig. 3 and summarized as follows:

$$\mathbf{w} = \text{MLP} \left(\left[\frac{16}{N} \sum_{i=1}^{N/16} \mathbf{F}^*[i, :] , N_0 \right] \right)$$

$$\mathbf{F}_{SA}^* = \underbrace{[\mathbf{w}, \dots, \mathbf{w}]^T}_{N/16} \odot \mathbf{F}^*. \quad (12)$$

We further note that one can also perform the mean pooling operation along the second axis; however, simulation results show that the presented scheme is strictly better. This aligns with the analysis in [3]; since the points within a point cloud are unordered, calculating the average over $\frac{N}{16}$ points means that the result would not be effected much from the input order of the points in the point cloud. The SA block at the SEPT decoder follows exactly the same processing, and is omitted here due to page limit.

IV. OTA-NeRF FRAMEWORK

The SEPT model presented in the previous section is designed to transmit small point clouds. However, its performance is limited when the input point cloud has a large number of points. This is due to the fact that the max-pooling operation at the SEPT encoder causes substantial loss of details. In this section, we introduce a hybrid point cloud transmission scheme, dubbed OTA-NeRF, which is capable to transmit point clouds of arbitrary size.

A. Representing Point Clouds via Neural Networks

In this subsection, we first introduce the underlying principle of the OTA-NeRF framework that the data samples such as images and point clouds, can be represented using neural networks [12], [14]. We start with the training and testing procedures of the OTA-NeRF without considering the noise introduced by the wireless channel.

1) *Point cloud preprocessing:* As before, we focus on the transmission of geometric information, thus, we consider a point cloud $\mathcal{P} = \{\mathbf{X}, \mathbf{F}\}$, where \mathbf{F} is set to an all-ones vector. \mathcal{P} is first normalized within the range of $[0, 1]$, i.e., $\mathbf{x}_i \in [0, 1]^3, \forall i \in [1, N]$, where N is the number of points in \mathcal{P} .

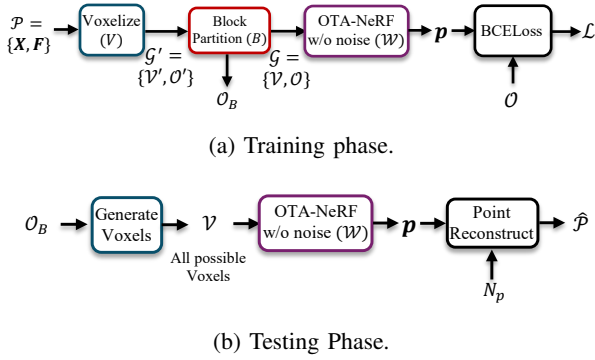


Figure 4: Illustrations of the training and testing phases of the proposed OTA-NeRF framework without noise.

Voxelization: Unlike images, where pixels lie on a regular grid, the points of a point cloud are distributed irregularly in the 3D space. To be consistent with the original NeRF framework, we partition the input point cloud \mathcal{P} into voxels. A uniform voxelization is adopted, where each unit interval along the x, y and z axes is equally partitioned into 2^V segments. As a result, 2^{3V} number of voxels are obtained and each voxel is represented by its indices, $(i, j, k); i, j, k \in [1, 2^V]$ corresponding to the (i, j, k) -th segment along the x, y and z axes, respectively.

Similar to the Octree representation [17], a voxel is occupied if there exists at least one point in it. By traversing over all the voxels, the original point cloud, \mathcal{P} , is transformed into a discrete representation, denoted as $\mathcal{G}' \triangleq \{\mathcal{V}', \mathcal{O}'\}$, where \mathcal{V}' denotes all the 2^{3V} voxels with indices ranging from $(1, 1, 1)$ to $(2^V, 2^V, 2^V)$. The occupancy information of \mathcal{V}' is represented by \mathcal{O}' , whose (i, j, k) -th element, $\mathcal{O}'_{i,j,k} \in \{0, 1\}$, indicates whether the voxel with indices, (i, j, k) , is occupied or not. Finally, we denote the number of occupied voxels as N_o .

Block Partition: In general, the discrete representation, \mathcal{G}' is sparse, i.e., $N_o \ll 2^{3V}$, which motivates us to remove the regions which are empty. To be precise, we partition the voxels \mathcal{V}' uniformly into 2^{3B} , ($B < V$) blocks where each block contains $2^{3(V-B)}$ voxels. If none of the voxels within the block are occupied, then we mark it as an empty block. The voxels belonging to the empty blocks are pruned from \mathcal{V}' and the voxels of the remaining occupied blocks are denoted by \mathcal{V} with cardinality $N_V \triangleq N_B 2^{3(V-B)}$, where $N_B \in [1, 2^{3B}]$ is the number of occupied blocks. We further denote the block occupancy information by \mathcal{O}_B . Intuitively, the block partition is essential in improving the reconstruction efficiency as the occupancy of the voxels belonging to the empty blocks are no longer needed to be predicted. After preprocessing, the original point cloud is represented by:

$$\mathcal{G} \triangleq \{\mathcal{V}, \mathcal{O}, \mathcal{O}_B\}, \quad (13)$$

where \mathcal{O} represents the occupancy of the voxels within \mathcal{V} .

2) *Training the neural network:* Next, we train a neural network to represent the point cloud whose detailed architecture is shown in Fig. 5. In particular, the input to the neural network is a three-dimensional vector, $\mathbf{x} = (i, j, k)/2^V$, representing the x, y and z coordinates of the voxels belonging to \mathcal{V} . Instead

of directly feeding \mathbf{x} to the neural network, we first employ a positional embedding module proposed in [14] to transform it to a higher dimensional vector, denoted by $\tilde{\mathbf{x}}$:

$$\tilde{\mathbf{x}} = [\mathbf{x}, \sin(2^0 \pi \mathbf{x}), \cos(2^0 \pi \mathbf{x}), \dots, \sin(2^{L-1} \pi \mathbf{x}), \cos(2^{L-1} \pi \mathbf{x})], \quad (14)$$

where L is the number of different frequencies and the dimension of $\tilde{\mathbf{x}}$ is denoted by $d_{in} \triangleq 6L + 3$. Note that employing the positional embedding module provides a much richer representation to the subsequent layers compared with the original input \mathbf{x} , yielding a better performance.

The neural network shown in Fig. 5 is comprised of three learnable modules, namely, the feature extraction, residual blocks, and the final classification module. All these modules employ fully connected (FC) layers, layer normalization (LN) and non-linear activation functions. The feature extraction module transforms the input $\tilde{\mathbf{x}}$ to a feature vector, $\mathbf{f} \in \mathbb{R}^{d_1}$. N_r residual blocks with residual connections are employed to improve the classification accuracy. The final classification module is comprised of a FC layer followed by a sigmoid activation function to produce the corresponding probability value, p . The neural network is trained to minimize the BCE loss⁵ with a goal to correctly predict the occupancy of the voxels:

$$\mathcal{L} = \frac{1}{N_V} \sum_{v=1}^{N_V} -(o_v \log(p_v) + (1 - o_v) \log(1 - p_v)), \quad (15)$$

where N_V is the total number of voxels in \mathcal{V} and $o_v \in \{0, 1\}$ indicates if the v -th voxel is occupied or not.

3) *Point cloud reconstruction:* After training, we assume that the neural network weights, denoted by \mathcal{W} , and the block occupancy information, \mathcal{O}_B , are available at the decoder. The voxels, \mathcal{V} , are first regenerated using the block occupancy information, \mathcal{O}_B . Then, the coordinates of the voxels within \mathcal{V} are fed to the neural network with weights, \mathcal{W} , to obtain the probability vector, $\mathbf{p} \in (0, 1)^{N_V}$. We then sort the elements of \mathbf{p} and the voxels corresponding to the top- N_p probability values will be marked as occupied while the others are assumed to be empty. Note that N_p does not need to be the same with the number of occupied voxels in \mathcal{G} , i.e., N_o . As will be shown in the simulation part, choosing a proper N_p value is essential for a good reconstruction performance. In real implementations, the encoder generates different reconstructed point clouds, $\hat{\mathcal{P}}$, with different N_p values. The $D1$ performances of these reconstructed point clouds can be calculated by the encoder, and the N_p which yields the best $D1$ performance can be adopted and transmitted to the decoder as a hyper parameter. Finally, the overall training and testing processes for the OTA-NeRF model without noise are illustrated in Fig. 4.

B. Neural Network Weights Over-the-Air

In the previous subsection, we assume the weights, \mathcal{W} , of the OTA-NeRF model shown in Fig. 5 are perfectly available at the decoder side. This can be achieved by first applying

⁵We also tried the focal loss as the loss function [12]; however, BCE loss yields a better performance in our simulations.

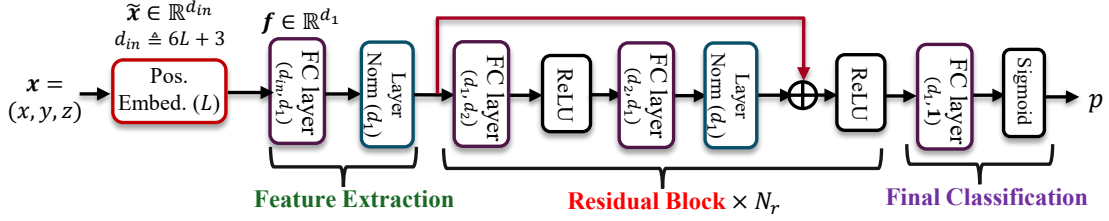
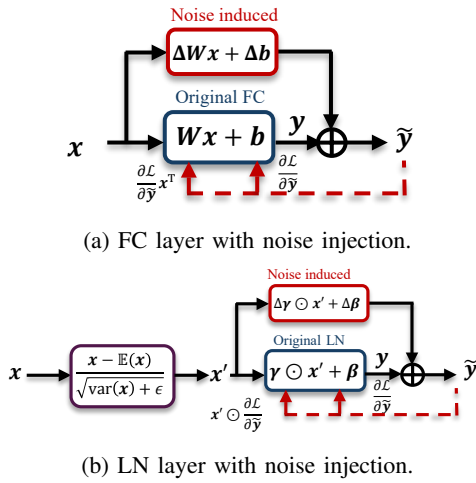


Figure 5: The neural network architecture of the OTA-NeRF model. In particular, the model is comprised of four modules, the positional embedding module, the feature extraction module, the residual blocks and the final classification module. The OTA-NeRF model takes the coordinate of a voxel as input and predicts if the voxel is occupied or not.



(a) FC layer with noise injection.

(b) LN layer with noise injection.

Figure 6: The forward and backward processes for both FC and LN layers with noise injection.

lossless source coding to transform \mathcal{W} into a bit sequence which is further channel coded and modulated to be transmitted over the channel. However, digital coded modulation suffers from cliff and leveling effects, which limit its performance when accurate channel estimation is no available. Therefore, we consider an alternative JSCC approach, namely, the OTA-NeRF framework, which is presented next.

As shown in Fig. 5, the proposed OTA-NeRF model is comprised of two different types of layers, namely, the FC and the LN layers, whose input-output relationships are expressed as:

$$\mathbf{y} = \mathbf{W}\mathbf{x} + \mathbf{b} \quad (16)$$

for the FC layer, and

$$\mathbf{y} = \frac{\mathbf{x} - \mathbb{E}(\mathbf{x})}{\sqrt{\text{var}(\mathbf{x}) + \epsilon}} \odot \boldsymbol{\gamma} + \boldsymbol{\beta} \quad (17)$$

for the LN layer. Here, $\text{var}(\mathbf{x})$ denotes the variance of the input vector \mathbf{x} , and ϵ is introduced for computational stability. We first assume the weights and the biases are transmitted over the AWGN channel (the algorithm is also applicable to fading channels). Take the FC layer as an example, the received signal at the receiver can be expressed as:

$$\tilde{\mathbf{W}} = \mathbf{W} + \Delta\mathbf{W},$$

$$\tilde{\mathbf{b}} = \mathbf{b} + \Delta\mathbf{b}, \quad (18)$$

where both $\Delta\mathbf{W}$ and $\Delta\mathbf{b}$ are the Gaussian noise components added to the original weights and biases, \mathbf{W} and \mathbf{b} , satisfying:

$$\begin{aligned} \|\mathbf{W}\|_F^2 &= \text{SNR} \mathbb{E}(\|\Delta\mathbf{W}\|_F^2), \\ \|\mathbf{b}\|_2^2 &= \text{SNR} \mathbb{E}(\|\Delta\mathbf{b}\|_2^2). \end{aligned} \quad (19)$$

The new input-output relationship of the FC layer with noise can be expressed as:

$$\tilde{\mathbf{y}} = \underbrace{\mathbf{W}\mathbf{x} + \mathbf{b}}_{\text{original } \mathbf{y}} + \underbrace{(\Delta\mathbf{W}\mathbf{x} + \Delta\mathbf{b})}_{\text{noise induced}}. \quad (20)$$

The training objective of OTA-NeRF is to obtain \mathbf{W} and \mathbf{b} that are robust to different $\Delta\mathbf{W}$ and $\Delta\mathbf{b}$ realizations. The update rule of \mathbf{W} and \mathbf{b} can be expressed as:

$$\begin{aligned} \mathbf{W} &\leftarrow \mathbf{W} - \eta \frac{\partial \mathcal{L}}{\partial \tilde{\mathbf{y}}} \mathbf{x}^\top, \\ \mathbf{b} &\leftarrow \mathbf{b} - \eta \frac{\partial \mathcal{L}}{\partial \tilde{\mathbf{y}}}, \end{aligned} \quad (21)$$

where η is the learning rate. Note that compared with the original optimization procedure, where the gradient is $\frac{\partial \mathcal{L}}{\partial \mathbf{y}}$, we have $\frac{\partial \mathcal{L}}{\partial \tilde{\mathbf{y}}}$ due to the noise in the forward process.

The update rule for $\boldsymbol{\gamma}$ and $\boldsymbol{\beta}$ of the LN layer follows similarly to (21):

$$\begin{aligned} \boldsymbol{\gamma} &\leftarrow \boldsymbol{\gamma} - \eta \mathbf{x}' \odot \frac{\partial \mathcal{L}}{\partial \tilde{\mathbf{y}}}, \\ \boldsymbol{\beta} &\leftarrow \boldsymbol{\beta} - \eta \frac{\partial \mathcal{L}}{\partial \tilde{\mathbf{y}}}, \end{aligned} \quad (22)$$

where $\mathbf{x}' = \frac{\mathbf{x} - \mathbb{E}(\mathbf{x})}{\sqrt{\text{var}(\mathbf{x}) + \epsilon}}$.

The forward and backward processes of the noisy FC and LN layers during training are summarized in Fig. 6. After training, we obtain the neural network weights, \mathcal{W} , which will be transmitted to the receiver directly over the noisy channel without any further coding. The block occupancy information, \mathcal{O}_B , and the number of reconstructed points, N_p , on the other hand, are protected by ultra-reliable channel codes, and are assumed to be available at the decoder side. It is worth mentioning that, the N_p value is determined via simulations at the transmitter analogous to that in [25]. In particular, for a specific N_p value, the encoder calculates the average D1 performance for a large number of noise realizations, and selects the N_p value that results in the best average

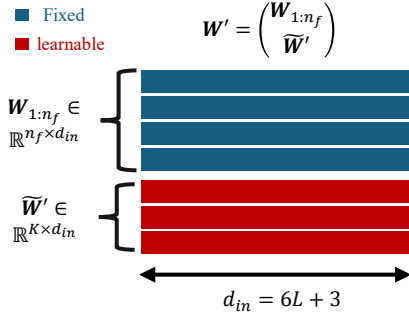


Figure 7: We fix n_f rows/elements of the weight (\mathbf{W}) / bias (\mathbf{b}) while update the remaining K rows/elements to obtain the weight and bias, \mathbf{W}' and \mathbf{b}' , for point cloud \mathcal{P}' .

D1 performance. The training and testing processes of the proposed OTA-NeRF model are summarized in Algorithm 1.

C. Fine-tuning for Bandwidth Efficiency

In the previous subsection, a neural network with parameters \mathcal{W} is trained and transmitted over the noisy channel for a specific point cloud, denoted by \mathcal{P} . When a new point cloud, \mathcal{P}' , arrives, a new neural network with parameters, \mathcal{W}' , should be trained from scratch. Since the point clouds \mathcal{P} and \mathcal{P}' might share some features, it is possible to transmit less number of parameters for \mathcal{W}' given that \mathcal{W} is already available at the destination. In particular, we consider reducing the size and the number of training epochs to obtain \mathcal{W}' for \mathcal{P}' by fine-tuning only a small fraction of the weights of \mathcal{W} .

To start with, we emphasize that it is critical to determine which part of the parameters to freeze/fine-tune. For instance, one may update the parameters in the residual blocks while keeping the feature extraction and final classification modules fixed or one can fine-tune the parameters of the feature extraction module while leaving the remaining parameters frozen. We found through ablation experiments that it is more beneficial to update the parameters in the feature extraction and final classification modules, which consists of $d_{in}(d_1 + 1)$ and $(d_2 + 1)$ parameters, respectively. Since the number of parameters in the final classification module is relatively small, we will update all its $(d_2 + 1)$ elements. For the feature extraction module, on the other hand, we only fine-tune part of its FC layer.

Let $\mathbf{W} \in \mathbb{R}^{d_{in} \times d_1}$ and $\mathbf{b} \in \mathbb{R}^{d_1}$ denote the weight and the bias of the FC layer, respectively, and K control the number of parameters for fine-tuning. For the new point cloud, \mathcal{P}' , we fix the first $n_f \triangleq d_1 - K$ rows of \mathbf{W} and the first n_f elements of \mathbf{b} . The remaining K rows and K elements are replaced by the new values, $\widetilde{\mathbf{W}}' \in \mathbb{R}^{K \times d_{in}}$ and $\widetilde{\mathbf{b}}' \in \mathbb{R}^K$, respectively. The updated feature vector \mathbf{f}' for \mathcal{P}' can be expressed as:

$$\mathbf{f}' = \begin{bmatrix} \mathbf{W}_{1:n_f} \tilde{\mathbf{x}} + \mathbf{b}_{1:n_f} \\ \widetilde{\mathbf{W}}' \tilde{\mathbf{x}} + \widetilde{\mathbf{b}}' \end{bmatrix}. \quad (23)$$

The effective weight for the new point cloud is $\mathbf{W}' = \begin{bmatrix} \mathbf{W}_{1:n_f} \\ \widetilde{\mathbf{W}}' \end{bmatrix}$, while the effective bias is: $\mathbf{b}' = \begin{bmatrix} \mathbf{b}_{1:n_f} \\ \widetilde{\mathbf{b}}' \end{bmatrix}$. Both of

them are shown in Fig. 7 for a better illustration.

Since the parameters of the residual blocks are fixed, the number of real channel uses to transmit the neural network weights for \mathcal{P}' is simply $(d_{in} + 1)K + d_1 + 1$. By changing $K \in [0, d_1]$, different bandwidth and reconstruction performances can be obtained at the receiver. We will show through experiments that the proposed fine-tuning scheme is capable of achieving satisfactory reconstruction performance while using less channel bandwidth.

Algorithm 1: Training and evaluation algorithm for the proposed OTA-NeRF framework.

Input : $\mathcal{P}, V, B, L, N_{epoch}, \eta, \text{SNR}$

Output: $\hat{\mathcal{P}}, \mathcal{W}$

```

1  $\mathcal{G}' \leftarrow \text{Voxelization}(\mathcal{P}, V)$ 
2  $\mathcal{G} \triangleq \{\mathcal{V}, \mathcal{O}, \mathcal{O}_B\} \leftarrow \text{BlockPartition}(\mathcal{G}', B)$   $\triangleright$ 
   Point cloud preprocessing.
3 %% Training Phase.
4 for  $n = 1$  to  $N_{epoch}$  do
5   for Each batch  $x \in \mathcal{V}$  do
6      $\tilde{\mathbf{x}} =$ 
7        $[\mathbf{x}, \sin(2^0 \pi \mathbf{x}), \cos(2^0 \pi \mathbf{x}), \dots, \sin(2^{L-1} \pi \mathbf{x}),$ 
8          $\cos(2^{L-1} \pi \mathbf{x})]$ ,  $\triangleright$  Positional embedding.
9      $\widetilde{\mathcal{W}} \leftarrow \mathcal{W} + \Delta \mathcal{W}$   $\triangleright$  Noisy channel.
10     $\mathbf{p} \leftarrow \text{OTANeRFForward}(\{\mathcal{V}, \widetilde{\mathcal{W}}\})$ .
11    Calculate  $\mathcal{L} =$ 
12       $\frac{1}{N_V} \sum_{v=1}^{N_V} -(o_v \log(p_v) + (1 - o_v) \log(1 - p_v))$ .
13    for weights  $\in \mathcal{W}$  do
14      if  $\text{IsFCLayer}(\text{weights})$  then
15        Update  $\{\mathbf{W}, \mathbf{b}\}$  via Equ. (21);
16      else
17        Update  $\{\gamma, \beta\}$  via Equ. (22);
18  %% Evaluation Phase.
19   $N_p \leftarrow \text{SimulateBestNp}(\mathcal{W}, \text{SNR})$ .
20  Transmit  $\mathcal{W}$  with analog transmission and  $\mathcal{O}_B, N_p$ 
   with digital transmission.
21   $\mathcal{V} \leftarrow \text{GenerateVoxel}(\mathcal{O}_B)$ .
22   $\mathbf{p} \leftarrow \text{OTANeRFForward}(\mathcal{V}, \hat{\mathcal{W}})$ .
23   $\hat{\mathcal{P}} \leftarrow \text{PruneVoxel}(\mathbf{p}, N_p)$ .
```

V. NUMERICAL EXPERIMENTS

This section presents the results of our numerical experiments to evaluate the reconstruction performance of the proposed SEPT and the OTA-NeRF frameworks.

A. Evaluation of SEPT

SEPT is proposed mainly for small point clouds and we consider transmitting the point cloud data from the down-sampled ShapeNet dataset [36], which contains about 51000 different shapes, and each point cloud is sampled to $N = 2048$ points using the FPS algorithm. In both the SEPT encoder and decoder, the dimension of the intermediate attributes is set to

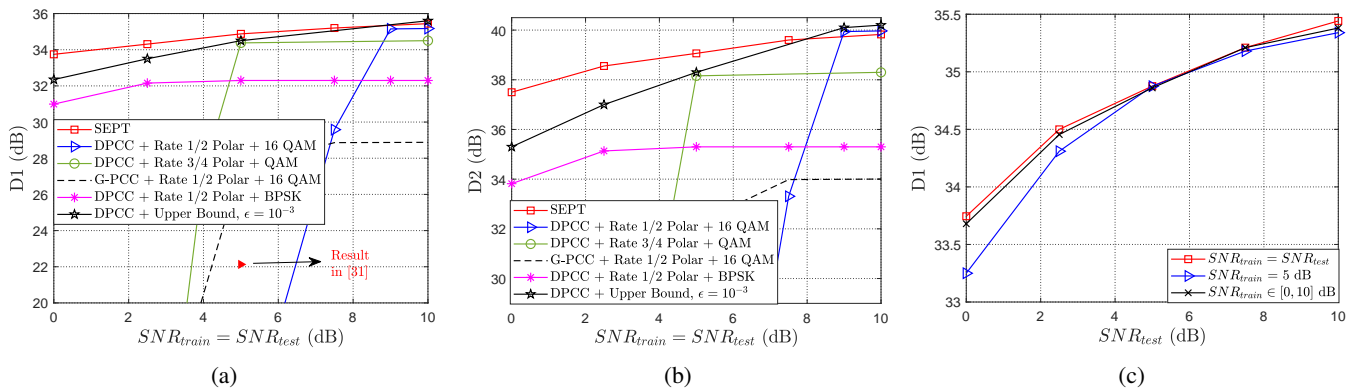


Figure 8: Performance comparison over an AWGN channel: (a) & (b) the D1 and D2 performances, where $n = 100$; (c) D1 versus SNR_{test} obtained by the SNR-adaptive SEPT model trained with $\text{SNR}_{\text{train}} \in [0, 10]$ dB and $n = 100$.

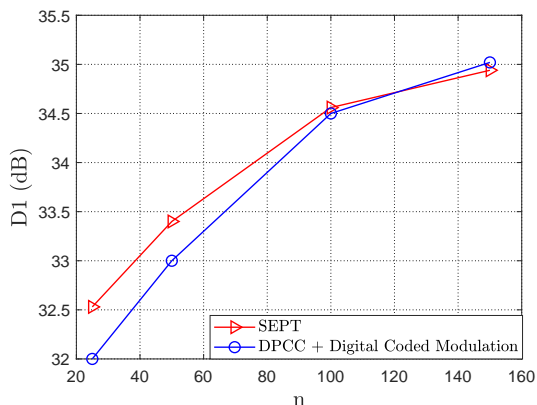


Figure 9: The D1 performance of the proposed SEPT w.r.t. different number of channel uses n over a Rayleigh fading channel with an average SNR of 10 dB.

$d_f = 256$ and the number of neurons in the MLPs of the coordinate reconstruction layer is set to 128. During training, we adopt the Adam optimizer with a varying learning rate, which is initialized to 0.001 and reduced by a factor of 0.5 every 20 epochs. We set the number of epochs to 200 and the batch size to 32.

1) *The reconstruction performance:* We first evaluate the reconstruction performance of SEPT with various channel SNR values over the AWGN channel. Two separate source-channel coding schemes are considered as benchmarks. For source coding, the first benchmark uses the standard octree-based point cloud compression scheme, i.e., G-PCC. The second benchmark, named DPCC, uses the state-of-the-art deep learning-based point cloud compression scheme with a focus on ultra low rate point cloud compression, [11]. Both schemes are protected by Polar codes with rate $\{1/2, 3/4\}$ and modulated by BPSK, QPSK, or 16QAM for transmission. We also provide the results for the DPCC delivered at the finite block length converse bound [37] for a block error rate of $\epsilon = 10^{-3}$.

The simulation results are presented in Fig. 8, where we fix the channel bandwidth to $n = 100$. In Figs. 8(a) and (b), a specific SEPT model is trained for each channel SNR value. As

shown, SEPT is significantly better than the separation based scheme with G-PCC. In particular, to obtain the results for G-PCC, we use an average of $n = 430$ in the simulations. Despite the much larger channel bandwidth compared with that used by SEPT, G-PCC is still much worse in terms of $D1$ performance. This observation is also reported in [11]. SEPT also outperforms the separation-based scheme with DPCC [11], especially in the low-SNR regime. Note that DPCC can approach the performance of SEPT at high SNRs, if proper code rate and modulation schemes are selected. We observe that the performance of the separation-based scheme with DPCC falls short of the performance of SEPT at low SNR values even if we consider the finite-rate upper bound from [37]. This can be considered as the best performance separation-based schemes can achieve in combination with state-of-the-art point cloud compression scheme DPCC. Another deep learning based point cloud transmission scheme is proposed in [31], where a graph neural network (GNN) is adopted as the backbone to extract the features from the original point cloud at the transmitter, while simple FC layers are employed for point cloud reconstruction at the receiver. We reproduce the results in [31] and for the scenario with $n = 100$ and $\text{SNR} = 5$ dB, it reports an average $D1$ value of 22.13 dB, whereas SEPT achieves 34.88 dB.

Next, we illustrate the benefits of the proposed SA blocks for SNR-adaptive transmission. In this simulation, the SNR-adaptive SEPT model is trained with $\text{SNR}_{\text{train}} \in [0, 10]$ dB and tested under $\text{SNR}_{\text{test}} = \{0, 2.5, 5, 7.5, 10\}$ dB. As shown in Fig. 8(c), the SNR-adaptive SEPT model can achieve nearly the same performance with models trained and tested at the same SNR, showing the effectiveness of the proposed SA blocks. We also observe that, even though when tested at $\text{SNR}_{\text{test}} = 0$ dB, the model trained at $\text{SNR}_{\text{train}} = 5$ dB achieves an average $D1$ value approximately 0.5 dB below that of the model trained under $\text{SNR}_{\text{train}} = \text{SNR}_{\text{test}}$, unlike digital coding approaches, the former model avoids the cliff and leveling effects when evaluated at different SNR values.

We then show the effectiveness of the SEPT over the Rayleigh fading channel as shown in Fig. 9. In this simulation, CSI h is sampled from a complex Gaussian distribution, $\mathcal{CN}(0, 1)$, and the average channel SNR is fixed at 10 dB. We evaluate the performance of the proposed SEPT w.r.t.

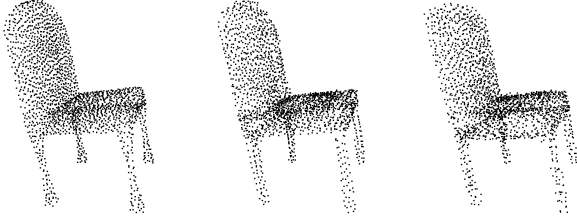


Figure 10: Visualization of reconstructed point clouds. Left: original \mathcal{P} ; middle: $\hat{\mathcal{P}}$ with $n = 150$, SNR = 5 dB; right: $\hat{\mathcal{P}}$ with $n = 150$, SNR = 0 dB.

different number of channel uses, n . The digital baseline in this case uses DPCC [11] for compression and a combination of coded modulation schemes for transmission. To be specific, we search over different combinations of 64QAM + 1/2 Polar, 16QAM + 1/2 Polar, 4QAM + 1/2 Polar and BPSK + 1/2 Polar, and use the option with the best performance at each channel realization. We can observe that the average $D1$ performance of SEPT outperforms the digital baseline by 0.5 dB in the short block length regime of $n = 25$. The two schemes perform similarly, and they both start to saturate beyond $n \geq 100$ due to the fact that the max pooling operation at the transmitter focuses more on the global features while the fine details may be lost.

We also provide a visualization of the reconstructed point clouds with $n = 150$ and SNR $\in \{0, 5\}$ dB. As shown in Fig. 10, SEPT yields visually pleasing results even when the SNR is as low as 0 dB.

B. Evaluation of OTA-NeRF

We then evaluate the reconstruction performance of the proposed OTA-NeRF scheme. Here, we consider the Semantic KITTI dataset [36], which is a large-scale outdoor-scene dataset for point cloud semantic segmentation.

Different combinations of the number of frequencies, L , hidden neurons, d_1, d_2 , and the residual blocks, N_r , are adopted to achieve different number of channel uses and reconstruction performances. The Adam optimizer with a varying learning rate is adopted where the learning rate is initialized to 10^{-3} and decreases by 0.1 every 30 epochs. The OTA-NeRF model is trained for 100 epochs with a batch size of 4096.

1) *Effects of the number of reconstructed points:* We first illustrate that the number of the reconstructed points, N_p , plays an important role in achieving satisfactory reconstruction performance. In this simulation, we set the neural network parameters, $(L, d_1, d_2, N_r) = (6, 32, 8, 1)$. The numbers of voxels and blocks per dimension are set to $(2^V, 2^B) = (128, 4)$, respectively, which leads to a discrete representation, \mathcal{G} with the numbers of occupied voxels and blocks equal to $(N_o, N_B) = (9363, 23)$, respectively. We consider an AWGN channel with SNR = $\{0, 5, 10\}$ dB and the OTA-NeRF model is trained and evaluated on the first point cloud from the dataset as an example. The average $D1$ performance w.r.t. N_p is shown in Fig. 11.

As can be seen, in the considered scenario, having $N_p > N_o$ yields better performance. It is also shown that when SNR is

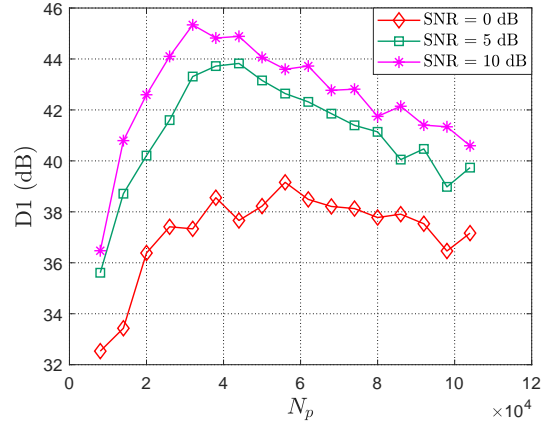


Figure 11: The average $D1$ performance of OTA-NeRF w.r.t. different number of reconstructed points, N_p .

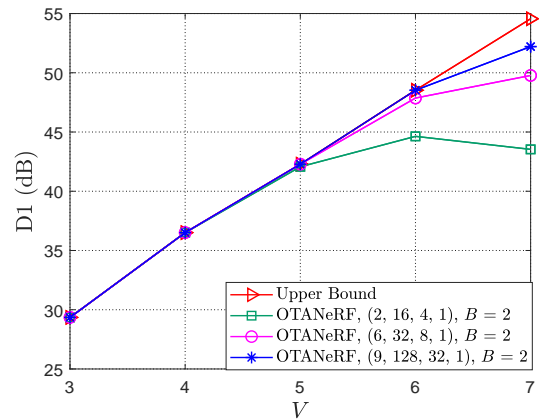


Figure 12: The $D1$ performance w.r.t. different voxel resolutions, V with fixed block resolution, $B = 2$.

higher, e.g., SNR = 5, 10 dB, a smaller N_p is preferable. When SNR = 0 dB, on the other hand, a larger N_p leads to a better reconstruction performance. This aligns with the intuition that, when SNR is high, the occupancy of each voxel can be predicted more accurately and there is no need to reconstruct the points with relatively low probability values. As mentioned in the previous section, the optimal N_p value is figured out at the transmitter and is transmitted digitally along with the block occupancy information, \mathcal{O}_B , as metadata to the destination for reconstruction.

2) *Voxel and block resolution:* We then explore the effects on the voxel and block resolutions, i.e., V and B , respectively. In this simulation, we fix the block resolution $B = 2$ and vary $V \in [3, 7]$. Different OTA-NeRF models are trained and tested assuming noiseless channel with parameters $(L, d_1, d_2, N_r) = (2, 16, 4, 1)$, $(6, 32, 8, 1)$ and $(9, 128, 32, 1)$. Their $D1$ performances w.r.t. different V are shown in Fig. 12.

As can be seen, the ‘Upper Bound’ curve calculates the $D1$ performance between different discrete representation, \mathcal{G} , (with different V) and the original point cloud \mathcal{P} . It is shown that the performance improves with V , which aligns with the intuition that when V is small, the total number of voxels decreases leading to substantial loss of details in the original point cloud.

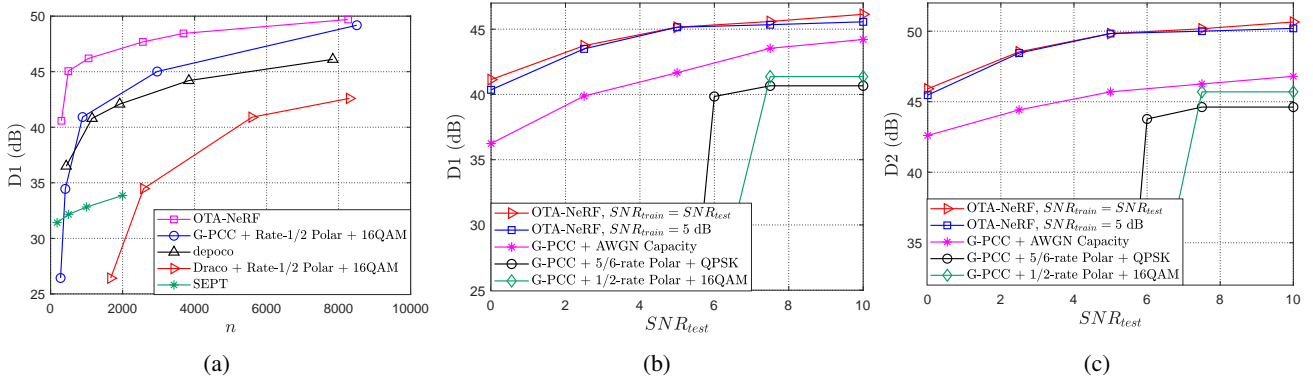


Figure 13: Reconstruction performances of the proposed OTA-NeRF scheme over the AWGN channel: (a) D1 obtained by the OTA-NeRF and various baseline schemes with different numbers of complex channel uses, n , under SNR = 10 dB; (b) & (c) D1 and D2 performances for different channel SNRs with a fixed number of complex channel uses.

Table I: The $D1$ performance, the number of voxels, $|\mathcal{V}|$, and the number of bits to represent \mathcal{O}_B w.r.t. different B .

Block resolution B	1	2	3
$D1$ (dB)	45.52	45.82	46.18
$ \mathcal{V} $	1.6×10^6	7.5×10^5	4.0×10^5
$3BN_B$	6	162	891

When V becomes larger, the original point cloud information is well preserved leading to a higher $D1$ value. We can also observe from the figure that for the OTA-NeRF model with parameters $(L, d_1, d_2, N_r) = (2, 16, 4, 1)$, its reconstruction performance first improves when $V \in \{3, 4, 5, 6\}$ and then degrades when $V = 7$. This is due to the fact that the number of voxels, $|\mathcal{V}|$, of the occupied blocks grows exponentially w.r.t V , and it is impossible for a neural network with a limited number of parameters to predict the occupancy of all the voxels correctly. This problem can be resolved by increasing the number of neural network parameters as the $D1$ performances of the OTA-NeRF models with $(L, d_1, d_2, N_r) = (6, 32, 8, 1)$ and $(9, 128, 32, 1)$ consistently improve with increasing V .

Then we investigate the effect of B for $V = 7$. As analyzed in Section IV, adopting a larger B value reduces the number of voxels within \mathcal{V} and thus improves the reconstruction quality as well as the processing efficiency at the receiver. This is verified in the simulations where three neural networks with parameters $(L, d_1, d_2, N_r) = (6, 32, 8, 1)$ are trained with different block resolutions, $B = \{1, 2, 3\}$ over the same point cloud in Fig. 12. The $D1$ performance, the number of voxels, $|\mathcal{V}|$, and the digital overhead to transmit the block occupancy information, \mathcal{O}_B , w.r.t. different B are provided in Table I.

As can be seen, with a large B , the reconstruction performance, $D1$, improves while the number of voxels, $|\mathcal{V}|$, reduces leading to a more efficient reconstruction process. However, the number of occupied blocks, N_B , grows rapidly with B leading to excessive digital overhead to transmit the block occupancy information, \mathcal{O}_B . In particular, suppose there are $N_B \leq 2^{3B-1}$ number of occupied blocks⁶, then, we need to transmit $3BN_B$

⁶When $N_B > 2^{3B-1}$, we will transmit the indices of the empty blocks instead.

Table II: $D1$ performances of the proposed OTA-NeRF framework and the G-PCC baseline as a function of the channel SNR over a Rayleigh fading channel.

SNR (dB)	5	7.5	10	12.5	15
OTA-NeRF (dB)	41.76	44.95	45.03	45.79	46.01
G-PCC baseline (dB)	36.92	38.01	38.93	40.05	40.72

bits to the receiver over the wireless channel, where $3B$ is the number of bits to represent the index of each block. To guarantee ultra reliable transmission over a wide range of channel SNRs would require introducing significant amount of redundancy, which in turn, increases the bandwidth cost of metadata. Thus, we adopt $B = 2$ to strike a balance between the reconstruction performance and the channel bandwidth.

3) *Comparison with benchmarks*: We compare the proposed OTA-NeRF model with both conventional and learning-based point cloud transmission baselines over the AWGN channel. In particular, the reconstruction performance is evaluated over 10 arbitrarily chosen point clouds where a neural network is trained and tested for each point cloud. We set SNR = 10 dB and six different numbers of channel uses are obtained by training OTA-NeRF models with parameters $(L, d_1, d_2, N_r) = (2, 16, 4, 1), (4, 16, 4, 2), (6, 32, 8, 1), (6, 64, 16, 1), (6, 64, 16, 2)$ and $(9, 128, 32, 1)$. The meta data containing the block occupancy information, \mathcal{O}_B , and the optimal number of reconstructed points, N_p , are transmitted using 1/2-rate Polar code with QPSK modulation for reliable transmission, which consumes 57 channel uses on average. We first consider two baselines using conventional point cloud compression algorithms, namely, Draco [38] and G-PCC [17], whose bit outputs are protected by rate-1/2 Polar code followed by 16QAM modulation. Two deep learning based baselines are implemented, the first one is the SEPT in Section III and the other is the ‘depoco’ proposed in [10].

As shown in Fig. 13(a), the proposed OTA-NeRF framework outperforms all baselines for $n \leq 8 \times 10^3$. However, its reconstruction performance improves slowly when $n > 4 \times 10^3$. This can be understood by the neural scaling laws [39], where the MLP can only achieve a small test error with a large

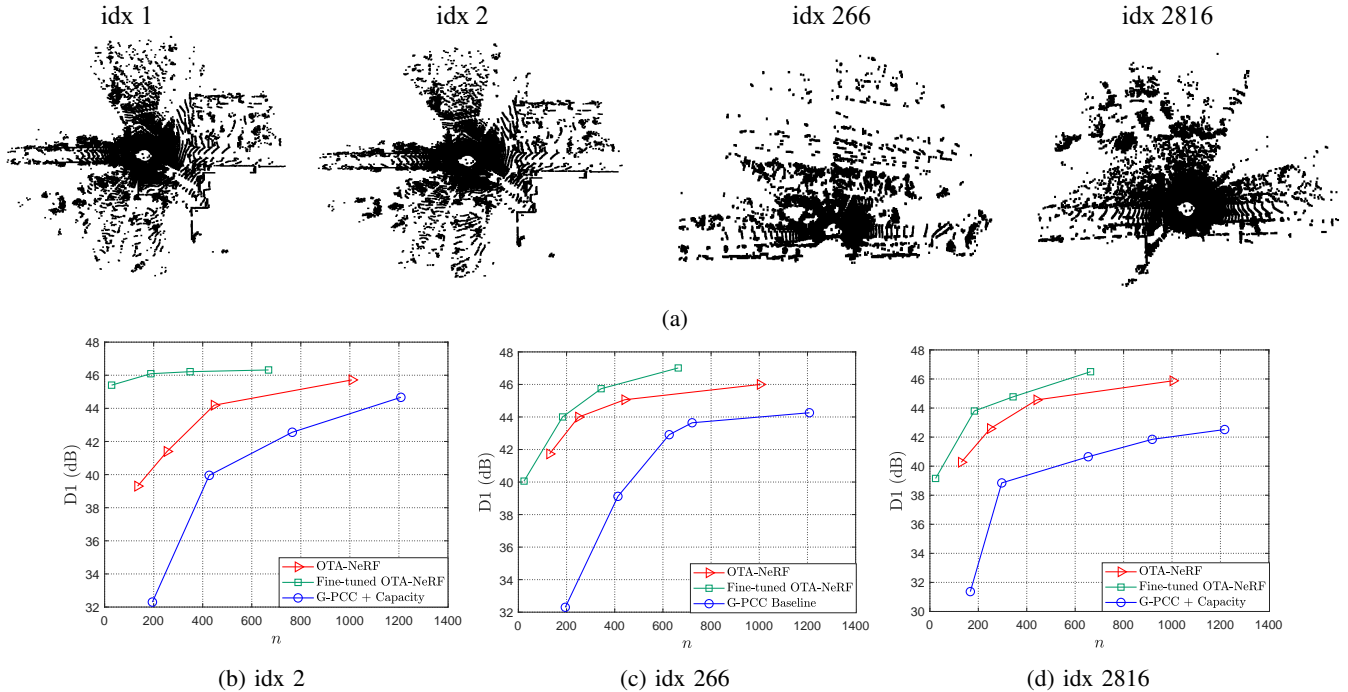


Figure 14: Performance comparison of the proposed OTA-NeRF schemes with/without fine-tuning and the G-PCC baseline delivered at AWGN channel capacity. The base model with parameters, $(L, d_1, d_2, N_r) = (6, 32, 8, 1)$, of the fine-tuning algorithm is trained on the point cloud with index 1 and evaluated on the point clouds with indices 2, 266 and 2816. Different fine-tuning parameters, $K = \{0, 8, 16, 32\}$, are considered. We also provide visualization of the point clouds with different indices.

number of parameters. It is also observed that though SEPT can achieve satisfactory reconstruction performance on the downsampled ShapeNet dataset with small number of points, it falls short when dealing with larger point clouds. This aligns with the intuition that the geometric information is lost due to the max-pooling operation leading to less satisfactory reconstruction performance. The depoco baseline transmits its downsampled coordinates using digital coded modulation, which not only achieves a lower $D1$ value on average, but also suffers from cliff and leveling effects.

We then show that OTA-NeRF is capable of achieving superior $D1$ and $D2$ performances at different SNR values. In this simulation, we compare the proposed OTA-NeRF model with the G-PCC baseline due to its superior reconstruction performance in Fig. 13(a), under $\text{SNR} = \{0, 2.5, 5.7.5, 10\}$ dB. In particular, we adopt a model with $(L, d_1, d_2, N_r) = (6, 32, 8, 1)$ which is comprised of 1993 learnable parameters. Rate-1/2 Polar code with BPSK modulation is adopted to transmit the meta data and the total number of complex channel uses is $n = 1111$. We also provide the $D1$ and $D2$ performances of the OTA-NeRF model trained at 5 dB while evaluated under different SNR values. For the G-PCC baseline, we consider transmitting its compression output using 1). rate-1/2 Polar code with 16QAM, 2). rate-3/4 Polar code with 16QAM and 3). the AWGN channel capacity. The relative performances of the aforementioned schemes are shown in Fig. 13 (b) & (c).

As can be seen, both $D1$ and $D2$ performances achieved

by the proposed OTA-NeRF models trained and tested at the same SNR outperform that of the G-PCC baselines adopting different coded modulation schemes and the AWGN channel capacity. Moreover, the OTA-NeRF model trained at fixed $\text{SNR} = 5$ dB yields satisfactory reconstruction performance when evaluated at other SNR values, which illustrates that it avoids the cliff and leveling effects. The G-PCC baseline with digital coded modulations, on the other hand, completely fails to reconstruct the original point cloud when the SNR drops below a certain threshold, and its performance saturates beyond this threshold.

We then evaluate the reconstruction performance of the OTA-NeRF scheme over Rayleigh fading channels. In this simulation, we set the neural network parameters for the OTA-NeRF model as $(L, d_1, d_2, N_r) = (6, 32, 8, 1)$. In the G-PCC baseline, the compressed bits are delivered at the ergodic capacity of the fading channel. Their reconstruction performances are shown in Table II. As can be seen from the table, the proposed OTA-NeRF scheme significantly outperforms the G-PCC baseline, even though the latter is assumed to communicate at the ergodic capacity.

4) *Results of fine-tuning*: Finally, we perform numerical experiments to illustrate the effectiveness of the proposed fine-tuning algorithm. In this simulation, we first train a base model on the first point cloud whose parameters are set to $(L, d_1, d_2, N_r) = (6, 32, 8, 1)$. The base model is assumed to be available to the receiver in advance and only the updated parameters need to be transmitted over the wireless channel for

different point cloud inputs as illustrated in Section IV-C. Due to the page limit, we show the effectiveness of the proposed fine-tuning algorithm using the point clouds with indices 2, 266 and 2816 over the AWGN channel. The SNR is set to 10 dB and the fine-tuning parameter is set to $K = \{0, 8, 16, 32\}$ leading to different numbers of complex channel uses. For the original OTA-NeRF models illustrated in Section IV-B, we consider four different sets of parameters, $(L, d_1, d_2, N_r) = (2, 8, 4, 1), (2, 16, 4, 1), (6, 16, 4, 1)$ and $(6, 32, 8, 1)$. The $D1$ performances obtained by the fine-tuning algorithm, the original OTA-NeRF model and the G-PCC baseline delivered at AWGN channel capacity are shown in Fig. 14.

As can be seen, for all the aforementioned point clouds, the $D1$ performance of the OTA-NeRF models with fine-tuning outperform the original ones trained from scratch. We can also observe from the figure that the gain obtained by the fine-tuning scheme over the original one varies from one point cloud to the next. This can be understood from the visualizations in Fig. 14: since the point cloud with index 2 is nearly identical to the one with index 1 for which the base model is trained, the reconstruction quality obtained even with $K = 0$ is good enough, and not much is gained by increasing K in this case. On the other hand, the point clouds with indices 266 and 2816 appear to be quite different, and hence, they require higher K values, but they are still more efficient compared to training a neural network from scratch.

VI. CONCLUSION

In this paper, we proposed two novel frameworks, namely, SEPT and OTA-NeRF, to enhance the quality of 3D point clouds when they are transmitted over bandwidth and SNR limited wireless links. For relatively small point clouds, the SEPT framework is shown to enable efficient, robust and SNR-adaptive delivery. For point clouds with arbitrary size, we propose the OTA-NeRF framework which encodes the point cloud data into the weights of a neural network which are transmitted directly over the wireless channel. A fine-tuning algorithm is proposed where only a fraction of the neural network weights are re-trained and transmitted which significantly reduces the bandwidth cost, particularly when there is correlation among the transmitted point clouds. Extensive numerical experiments are carried out to verify that both SEPT and OTA-NeRF frameworks achieve superior or comparable reconstruction performances w.r.t existing point cloud transmission schemes while mitigating the cliff and leveling effects, paving the way for realizing immersive user experiences in the metaverse, or collaborative sensing in vehicular networks.

Our study highlights two key challenges that merit further investigation:

- For the SEPT scheme, our findings indicate that the reconstruction performance reaches a saturation point as the number of channel uses increases. This implies that certain intricate details of the point cloud are not fully preserved during feature extraction. To address this issue, it is crucial to develop new encoding and decoding architectures that effectively capture these fine details, enabling progressive performance improvements with increasing channel bandwidth.

- A critical shortcoming of the OTA-NeRF framework is the high latency to train/fine-tune the base network, which may be undesirable for delay-sensitive applications. A possible solution is to employ a meta-network, which can be modulated according to the point cloud, similar to [40].

REFERENCES

- [1] C. Bian, Y. Shao, and D. Gündüz, "Wireless point cloud transmission," in *IEEE Int'l Wrksp. Signal Proc. Advances in Wireless Comms. (SPAWC)*, 2024.
- [2] R. B. Rusu and S. Cousins, "3D is here: Point Cloud Library," in *IEEE International Conference on Robotics and Automation*, 2011.
- [3] C. R. Qi, H. Su, K. Mo, and L. J. Guibas, "Pointnet: Deep learning on point sets for 3D classification and segmentation," in *CVPR*, 2017, pp. 652–660.
- [4] H. Zhao, L. Jiang, J. Jia, P. H. Torr, and V. Koltun, "Point transformer," in *ICCV*, 2021, pp. 16 259–16 268.
- [5] H. Thomas, C. R. Qi, J.-E. Deschard, B. Marcotegui, F. Goulette, and L. J. Guibas, "Kpconv: Flexible and deformable convolution for point clouds," in *CVPR*, 2019, pp. 6411–6420.
- [6] M.-H. Guo, J.-X. Cai, Z.-N. Liu, T.-J. Mu, R. R. Martin, and S.-M. Hu, "Pct: Point cloud transformer," *Computational Visual Media*, vol. 7, pp. 187–199, 2021.
- [7] C. Park, Y. Jeong, M. Cho, and J. Park, "Fast point transformer," in *Proceedings of the IEEE/CVF Conference on Computer Vision and Pattern Recognition*, 2022, pp. 16 949–16 958.
- [8] L. Huang, S. Wang, K. Wong, J. Liu, and R. Urtasun, "OctSqueeze: Octree-structured entropy model for LiDAR compression," in *CVPR*, June 2020.
- [9] J. Wang, D. Ding, Z. Li, and Z. Ma, "Multiscale point cloud geometry compression," in *2021 Data Compression Conference (DCC)*. IEEE, 2021, pp. 73–82.
- [10] L. Wiesmann, A. Milioto, X. Chen, C. Stachniss, and J. Behley, "Deep compression for dense point cloud maps," *IEEE Robotics and Automation Letters*, vol. 6, no. 2, pp. 2060–2067, 2021.
- [11] J. Zhang, G. Liu, D. Ding, and Z. Ma, "Transformer and upsampling-based point cloud compression," in *Proceedings of the 1st International Workshop on Advances in Point Cloud Compression, Processing and Analysis*, 2022, pp. 33–39.
- [12] H. Ruan, Y. Shao, Q. Yang, L. Zhao, and D. Niyato, "Point cloud compression with implicit neural representations: A unified framework," *arXiv:2405.11493*, 2024.
- [13] Y. Hu and Y. Wang, "Learning neural volumetric field for point cloud geometry compression," in *2022 Picture Coding Symposium (PCS)*, 2022, pp. 127–131.
- [14] B. Mildenhall, P. P. Srinivasan, M. Tancik, J. T. Barron, R. Ramamoorthi, and R. Ng, "NeRF: representing scenes as neural radiance fields for view synthesis," *Commun. ACM*, vol. 65, no. 1, p. 99–106, Dec 2021.
- [15] E. Dupont, A. Goliński, M. Alizadeh, Y. W. Teh, and A. Doucet, "Coin: Compression with implicit neural representations," *arXiv:2103.03123*, 2021.
- [16] S. Wiedemann, H. Kirchhoffer, S. Matlage, P. Haase, A. Marban, T. Marinč, D. Neumann, T. Nguyen, H. Schwarz, T. Wiegand, D. Marpe, and W. Samek, "Deepcabac: A universal compression algorithm for deep neural networks," *IEEE Journal of Selected Topics in Signal Processing*, vol. 14, no. 4, pp. 700–714, 2020.
- [17] D. Graziosi, O. Nakagami, S. Kuma, A. Zaghetto, T. Suzuki, and A. Tabatabai, "An overview of ongoing point cloud compression standardization activities: Video-based (V-PCC) and geometry-based (G-PCC)," *APSIPA Transactions on Signal and Information Processing*, vol. 9, pp. 1–13, 2020.
- [18] D. Gündüz, M. A. Wigger, T.-Y. Tung, P. Zhang, and Y. Xiao, "Joint source–channel coding: Fundamentals and recent progress in practical designs," *Proceedings of the IEEE*, pp. 1–32, 2024.
- [19] E. Boursoulatzé, D. B. Kurka, and D. Gündüz, "Deep joint source-channel coding for wireless image transmission," *IEEE Trans. Cognitive Commun. Netw.*, vol. 5, no. 3, pp. 567–579, 2019.
- [20] D. Gündüz, Z. Qin, I. E. Aguerri, H. S. Dhillon, Z. Yang, A. Yener, K. K. Wong, and C.-B. Chae, "Beyond transmitting bits: Context, semantics, and task-oriented communications," *IEEE J. Sel. Area Comm.*, 2022.
- [21] M. Yang, C. Bian, and H.-S. Kim, "OFDM-guided deep joint source channel coding for wireless multipath fading channels," *IEEE Trans. on Cogn. Comm. and Netw.*, vol. 8, no. 2, pp. 584–599, 2022.

- [22] H. Wu, Y. Shao, C. Bian, K. Mikolajczyk, and D. Gündüz, "Deep joint source-channel coding for adaptive image transmission over MIMO channels," *IEEE Transactions on Wireless Communications*, vol. 23, no. 10, pp. 15 002–15 017, 2024.
- [23] C. Bian, Y. Shao, H. Wu, E. Ozfatura, and D. Gündüz, "Process-and-forward: Deep joint source-channel coding over cooperative relay networks," *IEEE Journal on Selected Areas in Communications*, 2024.
- [24] J. Dai, S. Wang, K. Tan, Z. Si, X. Qin, K. Niu, and P. Zhang, "Nonlinear transform source-channel coding for semantic communications," *IEEE Journal on Selected Areas in Communications*, vol. 40, no. 8, pp. 2300–2316, 2022.
- [25] T.-Y. Tung and D. Gündüz, "DeepWiVe: Deep-learning-aided wireless video transmission," *IEEE Journal on Selected Areas in Communications*, vol. 40, no. 9, pp. 2570–2583, 2022.
- [26] S. Wang, J. Dai, Z. Liang, K. Niu, Z. Si, C. Dong, X. Qin, and P. Zhang, "Wireless deep video semantic transmission," *IEEE Journal on Selected Areas in Communications*, vol. 41, no. 1, pp. 214–229, 2023.
- [27] H. Xie, Z. Qin, G. Y. Li, and B.-H. Juang, "Deep learning enabled semantic communication systems," *IEEE Transactions on Signal Processing*, vol. 69, pp. 2663–2675, 2021.
- [28] M. Jankowski, D. Gündüz, and K. Mikolajczyk, "Airnet: Neural network transmission over the air," *IEEE Transactions on Wireless Communications*, vol. 23, no. 9, pp. 12 126–12 139, 2024.
- [29] Y. Huang, B. Bai, Y. Zhu, X. Qiao, X. Su, L. Yang, and P. Zhang, "Iscom: Interest-aware semantic communication scheme for point cloud video streaming on metaverse xr devices," *IEEE Journal on Selected Areas in Communications*, vol. 42, no. 4, pp. 1003–1021, 2024.
- [30] T. Fujihashi, T. Koike-Akino, T. Watanabe, and P. V. Orlik, "Holocast+: Hybrid digital-analog transmission for graceful point cloud delivery with graph fourier transform," *IEEE Transactions on Multimedia*, vol. 24, pp. 2179–2191, 2022.
- [31] T. Fujihashi, T. Koike-Akino, S. Chen, and T. Watanabe, "Wireless 3d point cloud delivery using deep graph neural networks," in *ICC 2021 - IEEE International Conference on Communications*, 2021, pp. 1–6.
- [32] T. Fujihashi, S. Kato, and T. Koike-Akino, "Implicit neural representation for low-overhead graph-based holographic-type communications," in *2024 IEEE International Conference on Acoustics, Speech and Signal Processing (ICASSP)*, 2024, pp. 2825–2829.
- [33] S. Xie, Q. Yang, Y. Sun, T. Han, Z. Yang, and Z. Shi, "Semantic communication for efficient point cloud transmission," *arXiv:2409.03319*, 2024.
- [34] J. Xu, B. Ai, W. Chen, A. Yang, P. Sun, and M. Rodrigues, "Wireless image transmission using deep source channel coding with attention modules," *IEEE Trans. on Circuits and Systems for Video Tech.*, 2021.
- [35] "Common test conditions for point cloud compression," *ISO/IEC JTC1/SC29/WG11 MPEG output document N19084*, Feb. 2020.
- [36] A. X. Chang, T. Funkhouser, L. Guibas, P. Hanrahan, Q. Huang, Z. Li, S. Savarese, M. Savva, S. Song, H. Su *et al.*, "Shapenet: An information-rich 3D model repository," *arXiv preprint arXiv:1512.03012*, 2015.
- [37] Y. Polyanskiy, H. V. Poor, and S. Verdú, "Channel coding rate in the finite blocklength regime," *IEEE Transactions on Information Theory*, vol. 56, no. 5, pp. 2307–2359, 2010.
- [38] Google, "Draco 3d data compression," <https://github.com/google/draco>.
- [39] J. Kaplan, S. McCandlish, T. Henighan, T. B. Brown, B. Chess, R. Child, S. Gray, A. Radford, J. Wu, and D. Amodei, "Scaling laws for neural language models," *arXiv preprint arXiv:2001.08361*, 2020.
- [40] E. Dupont, H. Loya, M. Alizadeh, A. Goliński, Y. W. Teh, and A. Doucet, "Coin++: Neural compression across modalities," *arXiv:2201.12904*, 2022.